Check for updates

Advanced Science

ADVANCED SCIENCE Open Access

www.advancedscience.com

RESEARCH ARTICLE OPEN ACCESS

Layer-by-Layer Solvent-Free Additive Manufacturing Enabling Controllable Ultrathick Electrode Coating for Lithium-Ion Battery

Tianlin Zhang[1] | Bharathkumar H. Javaregowda[1] | Prince M. Paul[2] | Ravi Trivedi[3,4] | Till Dreier[5] | Eduard Hryha[1] | Lars Nyborg[1] | Gao Liu[6] | Jinhua Sun[1]

[1]Materials and Manufacture Division, Department of Mechanical Engineering, Chalmers University of Technology, Göteborg, Sweden | [2]Centre For Computational Physics, Department of Science and Humanities, Faculty of Engineering, Karpagam Academy of Higher Education, Coimbatore, Tamil Nadu, India | [3]Department of Physics, Manipal University Jaipur, Jaipur, Rajasthan, India | [4]Centre for Quantum Materials, Devices & Technologies, Manipal University Jaipur, Jaipur, Rajasthan, India | [5]Excillum AB, Stockholm, Sweden | [6]Energy Technologies and Systems Division, Lawrence Berkeley National Laboratory, Berkeley, California, USA

Correspondence: Jinhua Sun (jinhua@chalmers.se)

Received: 4 August 2026 | **Revised:** 25 October 2026 | **Accepted:** 3 November 2026

Keywords: coating | electrical conductor | electrode | hot pressing | materials science | microstructure | nanotechnology | percolation

ABSTRACT

Dry electrode manufacturing is emerging as a transformative strategy for sustainable lithium-ion battery production, yet achieving ultrathick electrodes with homogeneous microstructures, efficient electron transport, and high electrochemical utilization remains a fundamental challenge. Here, we report a solvent-free, layer-by-layer additive manufacturing strategy that enables architecturally controlled ultrathick cathodes through molecular-level coupling between reduced graphene oxide (rGO) and binder. During roll-to-roll hot pressing, molten binder infiltrates the rGO framework to form a continuous conductive binder network, uniformly bridging NMC811 particles to enhance particle adhesion, suppress binder aggregation, and establish efficient electronic percolation. This strategy enables precise control of electrode thickness (300–1000 μm) and areal loading (20–100 mg cm^{-2}) while eliminating solvent-induced structural defects. The resulting multilayer cathodes, comprising up to five sequentially deposited layers, deliver a specific capacity of 230 mAh g^{-1} at 0.1 C and an areal capacity of ~10 mAh cm^{-2}. The nearly linear increase in areal capacity with layer number demonstrates homogeneous conductive networks and efficient electrochemical utilization throughout the electrode thickness. Electrodes with ~50 mg cm^{-2} loading retain 9 mAh cm^{-2} after 50 cycles. This work establishes a scalable platform for architecturally engineering ultrathick multilayer electrodes, overcoming heterogeneity of conventional thick electrodes and advancing next-generation high-energy-density lithium-ion batteries.

1 | Introduction

Given the global trend toward mitigating climate change through transportation electrification and wider energy transitions, there is an amplified demand for lithium-ion batteries (LIBs). This demand is expected to drive the LIB production chain to grow over 30% annually, potentially leading to a market size approaching 4.7 TWh [1]. In light of these developments and the ongoing pursuit of enhanced energy densities and performance, most of the research works have been focusing on the development of

Tianlin Zhang and Bharathkumar H. Javaregowda contributed equally to this work

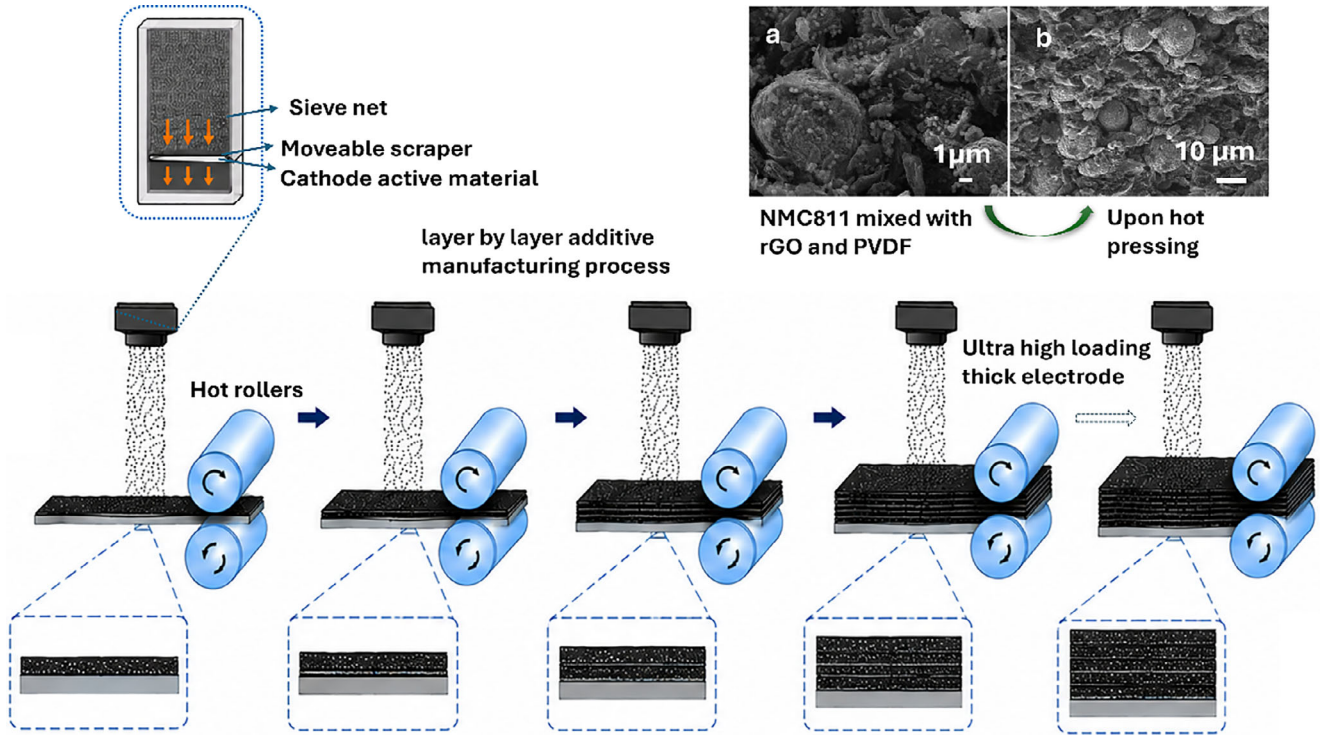
This is an open access article under the terms of the Creative Commons Attribution License, which permits use, distribution and reproduction in any medium, provided the original work is properly cited.
© 2026 The Author(s). *Advanced Science* published by Wiley-VCH GmbH

new electrode materials and electrolytes [2]. However, translating the advantages of the new electrode materials to the actual cell level is limited by the architectural constraints of the conventional wet-processed electrodes. Traditional wet coating processes employ N-Methyl-2-pyrrolidone (NMP) as a processing solvent for cathodes, which poses high environmental risk and economic challenges due to its toxic nature. The evaporation and drying process accounts for up to 11.5% of the overall battery production costs and 50% of the energy consumption of cell manufacturing, and leads to significant CO_2 emissions per kWh of LIB production [3–5]. Moreover, due to the drying sequence of NMP from the electrode surface to the deeper layers during the slurry drying process, it leads to difficulties in the simultaneous and uniform drying of each depth of the electrode. This leads to different degrees of sedimentation of the components of the electrode material, with heavier components settling at the bottom and lighter components such as carbon binder domains migrating to the surface via the evaporation of the solvent [6]. This results in uneven carbon binder distribution, which leads to delamination of the electrode materials from the current collector. In this context, dry electrode manufacturing offers a promising solution for more sustainable and cost-effective production of LIBs.

The solvent-free dry electrode manufacturing (DEM) process involves dry mixing of electrode materials, conductive additives, and binders, and applying them directly onto the current collector, thus eliminating the use of toxic NMP, which significantly reduces the environmental risks and overall production cost for cathode electrode manufacturing [7]. The commonly employed DEM techniques include electrostatic powder spray coating [8], hot pressing [9], vapor deposition [10], and roll-to-roll dry coating [11]. For instance, the electrostatic powder spraying technique was employed to produce dry $LiCoO_2$ (LCO) cathodes to uniformly distribute the cathode material onto the current collector, followed by hot pressing. However, due to the limited range of electrostatic attraction, fabricating thick and uniform electrodes remained a challenge. The study highlights the key observation that the PVDF binder promotes agglomeration and encapsulation of carbon black during hot pressing, impeding effective adhesion between active material particles [12]. Dry $LiNi_{0.8}Mn_{0.1}Co_{0.1}O_2$ (NMC 811) electrodes were fabricated via electrostatic spray technique, which showed stable electrochemical performance over 300 cycles, while the performance was comparable to the wet-processed NMC 811 [13]. Similarly, binder-less free-standing dry $LiFePO_4$ (LFP) electrodes were developed using holey graphene as a conducting additive, where the rate performance was comparable to that of conventional LFP cathodes [14]. However, this method necessitates the application of high pressures between 20 and 500 MPa, making it unsuitable for continuous roll-to-roll industrial production. Along with the processing technique, the conducting additive and the binder play an important role in realizing the full potential of dry processed electrode although their fraction is very less in the battery electrodes [15–17]. Currently, the DEM heavily depends on polytetrafluoroethylene (PTFE) binder due to its ability to fibrillate under shear and high chemical stability [18, 19]. However, PTFE production involves high CO_2 emissions, and it possesses high global warming potential [20, 21]. Additionally, due to its non-sticky nature, it requires a primer layer (CMC-SBR) via a wet process, and this conflicts with the solvent-free manufacturing process [22]. Furthermore, because PTFE is hydrophobic, electrolyte wettability is also an issue with highly loaded thick electrodes, and it gets irreversibly reduced below 1 V vs. Li/Li^{+}, which eliminates its use for dry manufacturing of negative electrodes [23–25]. When it comes to the roll-to-roll manufacturing of multi-layered free-standing dry electrodes, PTFE may not be an ideal choice due to its low mechanical strength [26]. Thus, it is necessary to choose the right combination of binder and conductive additive to produce thick electrodes with strong adhesion that preserves electrode integrity with high electron and ion percolating networks. Beyond the selection of suitable electrode constituents, the fabrication strategy is equally important for achieving uniform and mechanically stable ultrathick electrodes. In particular, directly processing a single thick powder layer can lead to nonuniform powder distribution, component segregation, and uneven heat and pressure transfer during compaction. These challenges become more pronounced as electrode thickness and areal loading increase. Therefore, a manufacturing approach that combines appropriate material interactions with improved control over powder deposition and electrode architecture is required to realize high-loading dry electrodes with interconnected electronic and ionic transport pathways.

Herein, we have strategically chosen reduced Graphene Oxide (rGO) as a conducting additive and PVDF as a binder to dry-process NMC 811 based on a layer-by-layer additive manufacturing method. Due to its high surface area and multi-layered structure combined with its high electrical conductivity, rGO is a promising alternative to carbon black, resulting in 3D conductive network in the dry-coated thick electrode. PVDF is chosen as a binder due to its excellent electrochemical stability over a wide operating voltage, compatibility with different electrolytes, and common use in cathode manufacturing. During hot pressing, rGO absorbs molten PVDF and establishes a strong adhesion with the active material, thus simultaneously serving conductive and adhesive roles, which are attributed to the high thermal conductivity of rGO. Furthermore, PVDF forms a strong intermolecular hydrogen-bonded network with rGO and NMC 811, ensuring high cohesive strength and resistance to cracking during repetitive charge–discharge cycles. The thickness of the dry-coated electrode could be controlled from 300 to 1000 µm by varying the loading from 20 to 100 mg/cm^2. The electrodes with multiple layers from 1 layer (1L) to 5 L with varying areal loading were tested, and their electrochemical performance was evaluated. The thickest cathode (5L) displayed an areal capacity of 20 mAh/cm^2. The investigation of the processing parameters and electrode structure on the electrochemical performance and stability of the fabricated high-loading thick cathodes demonstrates the practical feasibility of our solvent-free powder-stack layer-by-layer additive manufacturing approach by comparing the performance of the resulting high-loading NMC811 cathodes to those produced using conventional slurry-based methods. The dry-processed thick NMC811 delivered a high specific capacity of 220 mA h/g at 0.1 C and retained 90% of its initial capacity after 100 cycles. On the other hand, the wet-processed NMC811 delivered 150 mA h/g and showed 25% capacity fading after 100 cycles. Furthermore, electrodes with ~50 mg cm^{-2} retain an areal capacity >9 mA h cm^{-2} after 50 cycles. Thus, layer-by-layer deposition followed by hot compaction enables progressive electrode consolidation, reducing powder spreading and component segregation while improving heat and pressure transfer

21983844, 0, Downloaded from https://advanced.onlinelibrary.wiley.com/doi/10.1002/advs.78763 by Statens Beredning, Wiley Online Library on [16/11/2026]. See the Terms and Conditions (https://onlinelibrary.wiley.com/terms-and-conditions) on Wiley Online Library for rules of use; OA articles are governed by the applicable Creative Commons License



SCHEME 1 | Schematic representation of the fabrication process of multi-layered ultrathick cathodes through a solvent-free layer-by-layer additive manufacturing method. The inserted SEM images show the microstructure of the N8PrGO before (a) and after hot pressing (b).

within each layer. This architecture also provides greater control over additive distribution and the formation of the conductive–binding network, which can benefit electrode integrity and electrochemical performance. Accordingly, the proposed approach is not merely an alternative dry-electrode fabrication method, but a strategy for controlling pressure distribution, thermal exposure, binder flow, and particle packing during high-loading electrode manufacturing. The process also enables the fabrication of NMC811 electrodes with reduced binder contents of 5 wt.% and 2.5 wt.%, as well as $LiFePO_4$ (LFP) and $LiNi_{0.33}Mn_{0.33}Co_{0.33}O_2$ (NMC111) electrodes, all demonstrating stable electrochemical performance.

2 | Results and Discussion

The schematic illustration of the developed universal solvent-free additive manufacturing dry coating process for the fabrication of ultrathick electrodes with controllable thickness is depicted in Scheme 1. For the solvent-free electrode coating, the powder mixing is very important prior to the coating process. The NMC811 was thoroughly mixed with rGO (N8PrGO) using either ball milling or a high-shear mixer together with the PVDF. Taking advantage of the high surface area of rGO, the PVDF nanoparticles were absorbed on the surface of rGO (insert image in Scheme 1). For comparison, the NMC811 was also mixed with other conducting additives, including carbon black (CB) (N8PCB) and graphite nanoplatelet (GNP) (N8PGNP) in the presence of PVDF. The mixer was sieved using a mesh onto the current collector with uniform particle size at a constant flow rate to ensure uniform distribution. Subsequently, the powder was hot-pressed using heated rollers maintained at elevated temperatures (from 110°C to 180°C), where PVDF melts and is absorbed by high surface area rGO, forming the conductive binding network. As demonstrated in the inserted SEM images (Scheme 1), the PVDF particles disappeared after the hot-dry electrode processing. The high surface energy of 2D graphene allows the energy-favorable absorption of PVDF first (see the DFT calculation) and then coating on the surface of the NMC 811 particles. Since the binder and conductive additives interact at a molecular level, there is no phase separation once they bind to the active material particles. Taking the advantage of additive manufacturing for the multilayer coating, after the single-layer cathode film is formed by hot pressing, a second layer of the cathode film is created by spreading the electrode material again on the first layer and hot pressing to achieve a thicker cathode film.

This procedure is repeated to produce a cathode up to 5 layers. During the hot-pressing process, the pressure is adjusted to control the thickness and density of the pressed cathode film. Note: Taking advantage of the rGO, the porosity of N8PrGO could be easily controlled when compared to carbon black; under high pressure, the carbon black sample has very low porosity, which prevents the fast diffusion of the lithium ions. Opting for this layer of additional cathode powder rather than stacking pre-formed cathode material films on the cathode allows for the minimization of apparent interlayer interfaces and enhances the uniformity of the cathode. The NMC811 cathodes prepared with CB and rGO are labelled as N8PCB and N8PrGO, respectively.

One of the advantages of employing the solvent-free additive manufacturing for cathode fabrication is eliminating the sedimentation of the active material, carbon-binder domain migration, and electrode cracking during the drying process.

21983844, 0, Downloaded from https://advanced.onlinelibrary.wiley.com/doi/10.1002/advs.78763 by Statens Beredning, Wiley Online Library on [16/11/2026]. See the Terms and Conditions (https://onlinelibrary.wiley.com/terms-and-conditions) on Wiley Online Library for rules of use; OA articles are governed by the applicable Creative Commons License

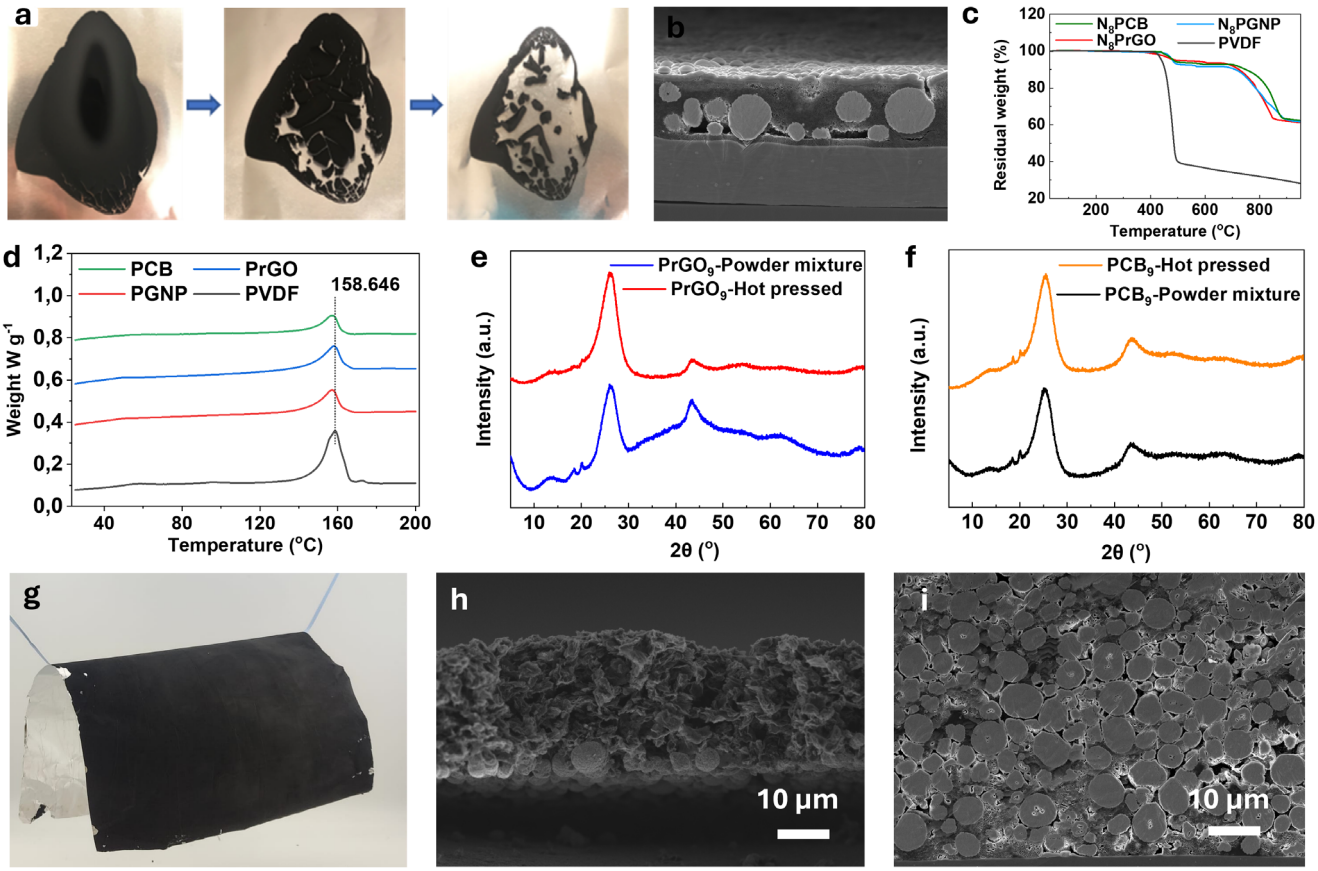


FIGURE 1 | (a) Image showing curling, cracking, and delamination phenomena during the drying process of 500 μm-thick slurry-coated cathode; (b) Cross-sectional SEM image of a slurry-coated N8PrGO cathode; (c) TGA profile for PVDF and the cathode powders mixed with CB, rGO, and GNP; (d) DSC analysis of PVDF with CB, rGO, and GNP; PXRD patterns of (e) $PrGO_9$ powder mixture and (f) PCB_9 powder mixture before and after hot pressing. (g) Photograph showing the dry-coated N8PrGO cathode; Cross-sectional SEM images of (h) slurry-processed and (i) dry-processed N8PrGO electrodes.

From Figure 1a, it is evident that in the case of conventional slurry-coated electrodes for the preparation of the thick electrode, the NMP solvent does not evaporate uniformly from the surface simultaneously but follows a drying sequence from the edges to the center. This not only challenges the maintenance of uniformity in the quantity and thickness of the electrode but also leads to material curling and delamination due to internal stress differences upon drying. In the direction perpendicular to the electrode surface, a similar discrepancy exists during the drying process from the electrode's surface to its interior, resulting in the stratification of different components within the cathode, which is revealed by the SEM image shown in Figure 1b. Heavier NMC particles settle at the bottom of the cathode, while conductive carbon and PVDF move to the surface via the evaporation of the high-viscosity NMP solvent, causing an uneven distribution of active material and additives in the cathode, thus diminishing the conductivity and adhesiveness of the cathode material.

One of the critical parameters in fabricating thick electrodes by hot roll pressing is identifying the appropriate hot-pressing temperature, which ensures the molecular-level interaction/absorption of the PVDF binder onto the surface of graphene. This will be the prerequisite that allows for effective binding with the active material and the additives while maintaining their chemical stability at high temperatures.

The Differential Scanning Calorimetry (DSC) thermogram shown in Figure 1d indicates that when PVDF is mixed with CB, GNP, and rGO, in a 1:1 mass ratio, the addition of these conductive additives influences the onset of melting temperature of PVDF. The melting onset of PVDF has slightly shifted to a lower temperature in the case of rGO, followed by CB and GNP. This is attributed to the high thermal conductivity and surface energy of rGO, which improves the heat transfer and alters the melting kinetics and crystallization behavior of PVDF [27]. It is known that the addition of a small amount of rGO induces a phase transformation of PVDF from a non-polar α-phase to a polar β-phase resulting from strong interaction between polar oxygen-containing moieties and defects on rGO and CF_2 groups of PVDF. These interactions altered the overall melting temperature of PVDF in the presence of rGO [27, 28].

On the other hand, the CB and GNP possess a weak Van der Waals interaction with the PVDF, and hence they display the least influence on the melting temperature and on the crystallinity of PVDF [29, 30]. The TGA analysis in Figure 1c confirms that all three components of the cathode maintain their chemical stability before reaching 400°C. Taking into account the heat transfer and dissipation processes during continuous hot-rolling and to ensure sufficient melting of PVDF in the inner layers of the thick cathode, a hot-pressing temperature of

21983844, 0, Downloaded from https://advanced.onlinelibrary.wiley.com/doi/10.1002/advs.78763 by Statens Beredning, Wiley Online Library on [16/11/2026]. See the Terms and Conditions (https://onlinelibrary.wiley.com/terms-and-conditions) on Wiley Online Library for rules of use; OA articles are governed by the applicable Creative Commons License

180°C is selected. Notably, the conductive additives CB, GNP, and rGO have enhanced the thermal stability of PVDF and its degradation temperature when compared to neat PVDF. To further demonstrate the superior reinforcement between PVDF and rGO during the hot-pressing process, a set of experiments was conducted, unlike the traditional mixing/blending of binder and conductive additive. Two samples were prepared by mixing PVDF with rGO or CB in a 1:9 mass ratio ($PrGO_9$ and PCB_9, respectively). These sets of samples don't contain NMC811, which excludes the influence of NMC811 on the thermal melting adsorption of PVDF onto the conductive additives. As shown in Figure 1e, the powder X-ray diffraction (XRD) patterns of the uniformly mixed $PrGO_9$ and PCB_9 show two intense diffraction peaks at $2\theta = 18.5°$ and 20.1° corresponding to the α and β phases of PVDF, respectively. Upon hot pressing the two powder mixtures at 180°C, the relative intensity of diffraction peaks of PVDF in $PrGO_9$ has significantly decreased, while the relative intensity of the rGO characteristic peak at $2\theta = 26°$ is enhanced. Furthermore, the peak at $2\theta = 20.1°$ has been slightly shifted to higher 2θ indicating that rGO induced phase transformation of PVDF to a more ordered β-phase with a complete disappearance of the α-phase of PVDF due to the strong interaction of the rGO sheet with the dipoles of PVDF [31]. This indicates that there exists a strong interaction between rGO and molten PVDF, resulting in high-quality electrodes with high conductivity. Contrastingly, the peak intensities of PVDF in PCB_9 remained unaltered, which is attributed to its poor interaction with PVDF, which in turn results in agglomerated electrode films with poor adhesion strength and conductivity (Figure 1f). Overall, replacing CB with rGO in the multilayer dry electrode processing inhibits PVDF agglomeration during the thermal melting recrystallization process, which is typically induced by carbon materials [29]. The PVDF particles have better wettability on the rGO surface due to the large surface energy and strong interaction between rGO and PVDF. The secondary PVDF particles that broke during the dry mixing process adhered to the surface of the rGO, followed by the coating on the NMC particles, which could enhance the structural strength of rGO and improve its adhesion with the active material while melting, resulting in a mechanically robust electrode structure. Figure 1g depicts the cathode prepared by a solvent-free method in large size (A4), maintaining strong adhesion via a strong interconnected network of NMC811, PVDF, and rGO without cracking even when bent. Characterization of the electrode cross-sections by SEM (Figure 1h,i) also reveals that the developed multilayer coating process ensures the fabrication of dry cathodes with high density and uniform material component distribution in the electrode; however, the wet-coated electrode shows the accumulation of the carbon additive and binder on the top surface of the electrode.

2.1 | Enhanced Interaction and Structural Reinforcement Between PVDF and rGO During the Dry Electrode Hot-Pressing Process

To understand the interactions and structural reinforcement between PVDF and rGO, the morphology of the mixed powder and the cross-sections of the hot-pressed electrodes were analyzed using SEM. The employment of an enhanced cross-rotary stirrer, equipped with additional blades, for a comprehensive duration of stirring directly on the raw material powder, facilitated thorough mixing and uniform distribution of the active material, binder, and conductive additive. Before hot pressing, PVDF was uniformly attached to the surface of NMC811 and mainly the conductive additive (Figure 2a) due to the strong surface energy of the rGO. The electrodes comprising CB and GNP showed aggregated films due to their low surface area and poor interactions with PVDF, resulting in uneven distribution of the binder throughout the electrode film (Figure 2b,c). This aggregation severely reduced the effective utilization of the conducting additives due to their extremely low contact area with the NMC 811 particles, which critically weakened both the binding and the conductivity of the cathode. Notably, the rGO-comprising electrode (Figure 2d) shows no aggregation upon melt pressing of PVDF, which is attributed to its high specific surface area, thermal conductivity, and 3D network formation through hydrogen bonding interactions between the rGO and PVDF, resulting in a high-quality electrode film. The self-organized rGO particles with micropores and large surface area could encapsulate the NMC particles within their 3D porous conductive network. During hot-pressing, the molten PVDF gets adsorbed strongly onto the rGO, thereby significantly enhancing the binding between rGO and the active material. Furthermore, the solidified PVDF reinforced the structural strength of the rGO. This is evident from the Raman spectrum and mapping of the dry 1L-thick electrodes, where the distribution of rGO was uniform throughout the electrode (Figure S1).

The EDS mapping (Figure 2e) shows the even distribution of all the components within the cathode architecture. The distribution of carbon (C) corresponds to the spatial distribution of rGO, revealing its excellent continuity within the cathode. The distribution of PVDF, Ni, Mn, Co and O in the dry electrode is evident from the EDS mapping. The rGO forms a continuous conductive network, encapsulating the NMC particles, thus providing enhanced electron transfer efficiency and utilization of the active material. Moreover, the high surface area and porous nature of the rGO could accommodate more electrolyte, which reduces the diffusion path for the lithium ions in the electrode, leading to fast charging–discharging characteristics of such a thick electrode. However, due to the nanoparticle feature of carbon black, the high density of the electrode after hot pressing leads to low porosity, limiting the diffusion of the lithium ions. The incorporation of rGO as the conductive filler in the cathode allows for a larger contact area between the active material and the binder by creating a percolation path for electron and ion diffusion throughout the cathode, resulting in improved adhesion and conductivity. The presence of PVDF is observed throughout the cathode, where PVDF exhibits a wider and more uniform distribution. Although the molten PVDF with lower molecular weight spreads and covers most of the NMC particles, only the PVDF in between the necking region connecting two neighboring NMC particles can provide effective binding. Thus, this approach has significantly enhanced the utilization efficiency of both the conductive additive and the binder. To further highlight the efficacy of our method in understanding the microstructure of the dry electrodes, the 3D X-ray laminographic scans of the 2L dry electrode were acquired. The bright features correspond to the active material particles, while the dark regions between the particles correspond to the pores or low-density phases of rGO/PVDF rich region. The reconstructed vertical laminography slices reveal a homogeneous particulate microstructure throughout the electrode thickness,

21983844, 0, Downloaded from https://advanced.onlinelibrary.wiley.com/doi/10.1002/advs.78763 by Statens Beredning, Wiley Online Library on [16/11/2026]. See the Terms and Conditions (https://onlinelibrary.wiley.com/terms-and-conditions) on Wiley Online Library for rules of use; OA articles are governed by the applicable Creative Commons License

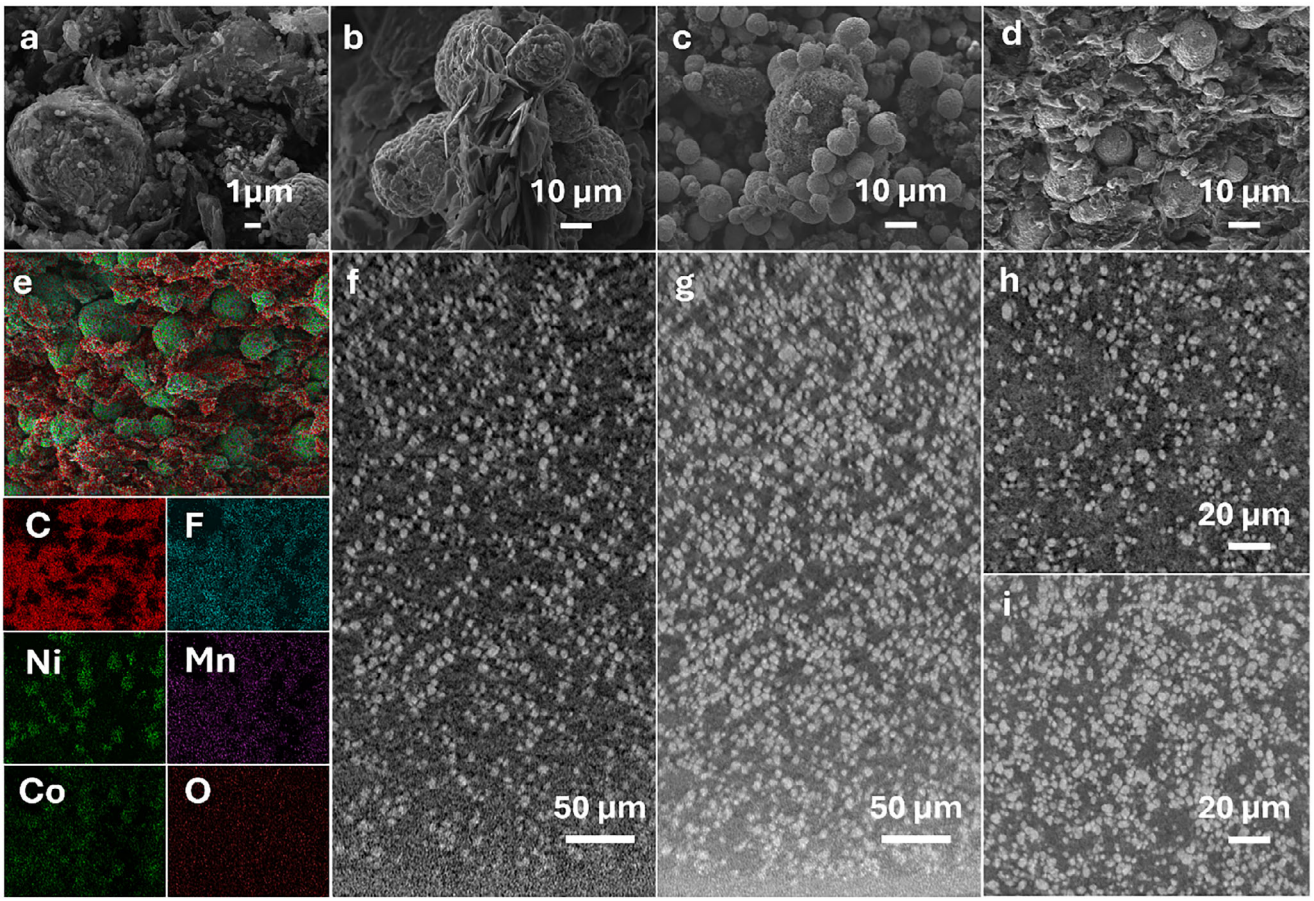


FIGURE 2 | SEM images of powder mixture of (a) N8PrGO,; (b) N8PGNP, (c) N8PCB. (d) SEM image of N8PrGO after hot pressing; The EDS mapping of N8PrGO showing (e) overlay of all the elements (C, F, Ni, Mn, Co and O). X-ray laminoscopic slices of N8PrGO dry electrodes with normal (f,h) and maximum intensity projection (g,i).

where the NMC811 particles are uniformly distributed without any cracks or interfacial voids. The continuous particle network suggests that there is a good interconnection between the particles through the rGO/PVDF network. Also, a slight increase in X-ray attenuation is visible near the current collector interface, indicating a locally enhanced particle packing and densification resulting from electrode compression (Figure 2f–i). Furthermore, no distinct separation between the sequentially deposited dry layers is observed, indicating effective interlayer consolidation during electrode fabrication and demonstrating that our layer-by-layer additive manufacturing process produces a structurally integrated electrode with a homogeneous electrode/rGO/PVDF network, which supports homogeneous pore distribution and electrolyte infiltration, which in turn improves Li-ion diffusion pathways.

To further demonstrate the effective interaction between PVDF and the graphene, density functional theory (DFT) calculations were employed. The optimized geometries of interaction between the graphene and the PVDF were analyzed at different temperatures to correlate with the experimental observations. For this, the optimized molecular structure of the β-phase of PVDF was selected, which shows the polar arrangement of the chains, allowing for a strong interaction with the carbon supports (Figure 3a). The optimized structure of a pristine sheet of graphene (Figure S6a) possesses typical top (T), bridge (B), and hollow (H) adsorption sites as the reference positions for subsequent adsorption studies.

Figure 3b illustrates a favorable conformation of β-PVDF on the graphene surface, and the binding energy was calculated to be −3.07 eV with an equilibrium separation of around 3.5Å indicating a thermodynamically stable adsorption controlled by van der Waals and electrostatic interactions. Furthermore, PVDF binding with extended graphene sheet 8 × 8 × 1 has also been shown in Figure 3b. AIMD simulations were employed to understand the interactions between PVDF and graphene at 25°C and 180°C. The snapshots shown in Figure 3c,d indicate the thermal stability of an isolated PVDF molecule and PVDF adsorbed on graphene. This magnitude of interfacial binding is attributed to the strong physisorption of polymeric binders to the graphene substrate, and this is similarly lower than analogous DFT results of binder-graphene interactions in battery materials and composite interfaces [32]. When multiple PVDF molecules are subjected to interact with graphene (Figure 3e), two isolated PVDF molecules interact at a noticeably much lower binding energy of −0.33 eV than their actual interaction with graphene, which is associated with the weak van der Waals-intermolecular forces. Furthermore, the interaction of PVDF on the graphene substrate was also analyzed at 180°C to match the experimental conditions, where the optimized geometries indicate a favorable binding interaction on the graphene sub-

21983844, 0, Downloaded from https://advanced.onlinelibrary.wiley.com/doi/10.1002/advs.78763 by Statens Beredning, Wiley Online Library on [16/11/2026]. See the Terms and Conditions (https://onlinelibrary.wiley.com/terms-and-conditions) on Wiley Online Library for rules of use; OA articles are governed by the applicable Creative Commons License

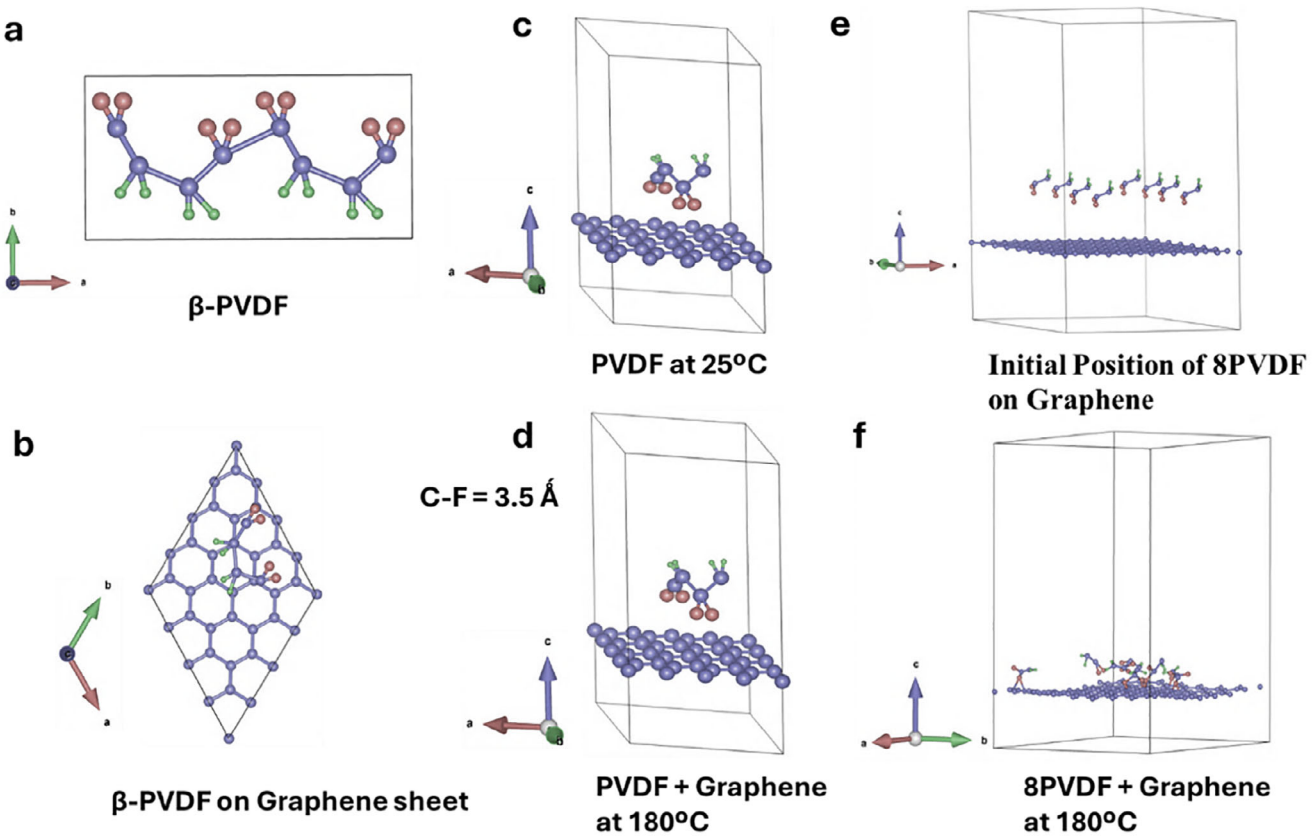


FIGURE 3 | (a) Optimized structure of PVDF; (b) PVDF interaction on graphene surface. AIMD snapshots at (c) 25°C and 180°C showing the thermal stability of an isolated PVDF molecule and PVDF adsorbed on graphene; (e) AIMD snapshots of graphene with increased PVDF loading in different orientations, illustrating stable interfacial coverage; and (f) polymer network formation at elevated temperature.

strate, resulting in the formation of a network of PVDF polymer (Figure 3f).

2.2 | Achieving High-Loading Thick Cathodes With Sustained High Capacity Through Dry Hot Pressing

Taking advantage of the additive multilayer coating, the thickness could be well controlled with each layer and also for the final electrode after the layer-by-layer dry-coating process. This is not possible with wet coating or direct spray coating (Figure 1a). In addition, the morphology of the electrode could also be controlled in such a multilayer coating process. We demonstrated the preparation of cathodes with different thicknesses ranging from 60 μm (slurry-coated) to beyond 1000 μm in solvent-free layer-by-layer processed cathodes. In the case of a continuous roll-to-roll hot pressing process, the thickness and loading in a single-layer electrode could be well controlled. Upon addition of more layers, the heat dessipation and melting of PVDF within the electrode could be enhanced, leading to improved adhesion between the NMC particles and the conductive additive. The strategy of multiple layer-by-layer additive manufacturing did not result in any interface between each layer coating, even in the multilayered ultrathick electrodes and allows for better control over electrode thickness and mass loading. It is imperative to note from the cross-section SEM images of the slurry-processed electrode (Figure 1b and 4a) that during solvent removal, PVDF migrates to the surface, resulting in electrode cracking and uneven particle distribution. On the other hand, the dry-processed electrodes show a densely packed electrode film with uniform distribution of NMC811, conducting additive, and PVDF. The cross-section SEM images of the dry NMC811 cathodes with different layers and the corresponding thickness of the electrodes are shown in Figure 4b–f. The electrode thickness and the number of layers in the dry electrodes have a linear relationship from 350 to 1150 um (Figure 4g).

The electrolyte wettability of multi-layered thick electrodes is important for understanding the cathode electrolyte interphase (CEI) formation, Li-ion tortuosity, and diffusion, which have significant influence on the rate capability of the electrode. The thick electrode prepared based on the conventional wet coating using carbon black as a conductive additive possesses poor electrolyte wettability and Li-ion diffusion. It is understood that in layer-by-layer manufactured electrodes, the Li-ion diffusion pathways are not always straight and will be influenced by electrolyte flow across the layers, and it is influenced by the nature of conducting additives and the thickness of the electrodes. Thus, the electrolyte sorption analysis of the wet and dry electrodes of NMC811 (1, 3, and 5L) was carried out using optical and Tensiometer measurements. For this, 1 M $LiPF_6$ electrolyte was dropped onto these electrodes, and the electrolyte absorption speed was noted as a function of time. Compared to wet electrodes, the dry electrodes displayed a faster electrolyte absorption, which is evident from the absorption speed (slopes)

21983844, 0, Downloaded from https://advanced.onlinelibrary.wiley.com/doi/10.1002/advs.78763 by Statens Beredning, Wiley Online Library on [16/11/2026]. See the Terms and Conditions (https://onlinelibrary.wiley.com/terms-and-conditions) on Wiley Online Library for rules of use; OA articles are governed by the applicable Creative Commons License

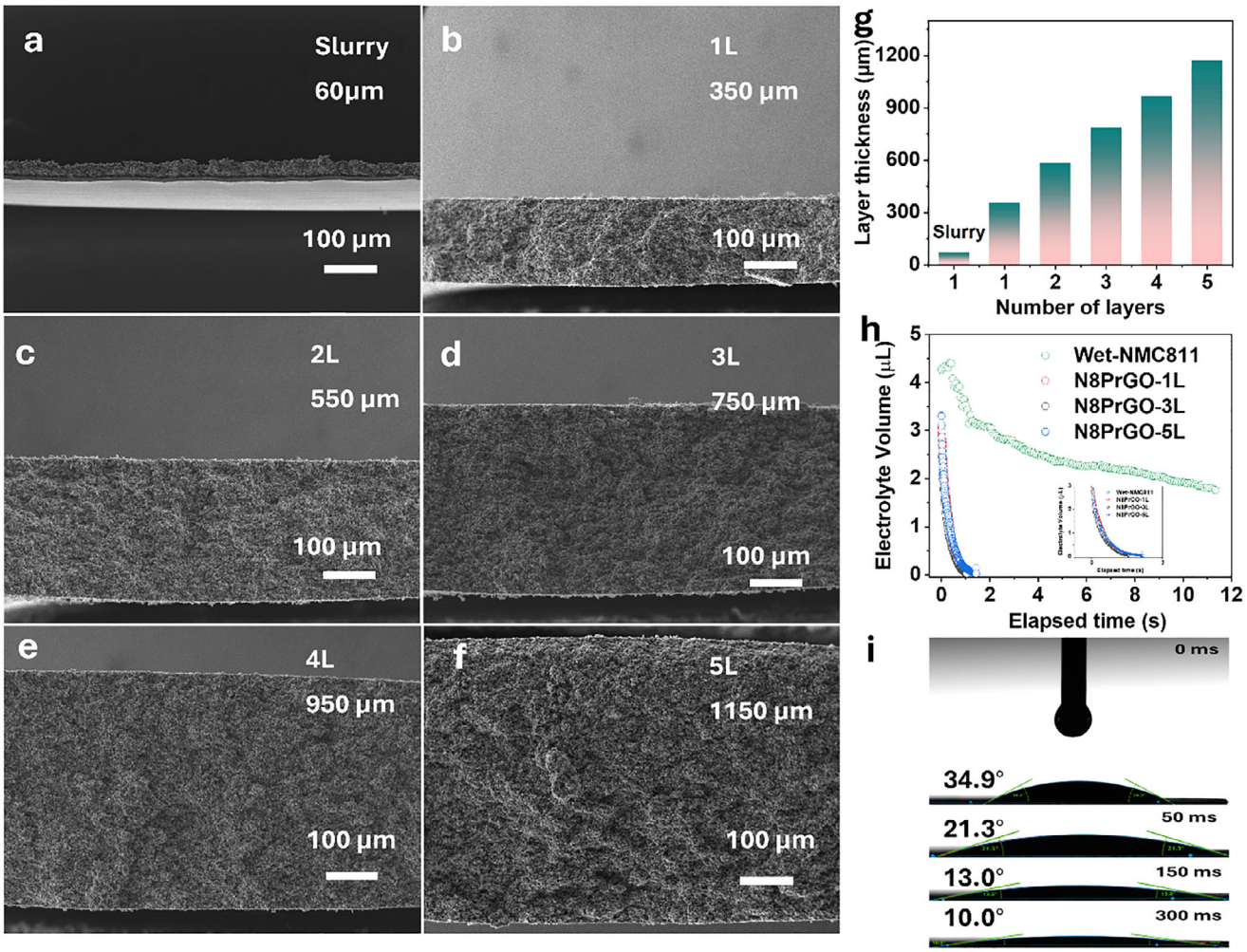


FIGURE 4 | Cross-sectional SEM image of NMP based slurry-coated NMC811 cathode (a) and solvent-free fabricated NMC811 cathodes with (b) 1L, (c) 2L, (d) 3L, (e) 4L and (f) 5L. The plot shows the variation of layer thickness of slurry and layered dry-coated cathodes (g); Electrolyte absorption of wet coated electrode and dry coated 1L–5L-thick electrodes (h); contact angle variation as the droplet diffuses into the 5L-thick electrode over 300 ms (i).

(Figure 4h), in agreement with the high surface area of the rGO (Figure S3a) and high porosity of the 5L electrode, which is nearly 52%. Figure S2a,b depict electrolyte absorption behavior of the dry electrodes as a function of areal mass loading and conducting additives respectively. The electrolyte uptake for 1L-5L electrodes is depicted in Figure S2c.

This indicates that the dry electrodes have better electrolyte uptake in a shorter time compared to the wet electrode. This enhanced electrolyte absorption of dry N8PrGO electrodes is attributed to the high specific surface area of rGO, which allows for better electrolyte infiltration, which in turn improves the Li-ion diffusion kinetics and the rate performance. Furthermore, the thick electrode comprising rGO absorbed more electrolyte when compared to those with GNP and PCB. The BET surface measurements further support this fact, where the N8PrGO electrode showed a specific surface area of 32.504 m^2/g while the N8PCB and N8PGNP had a specific surface area of 3.6 and 1.0 m^2/g, respectively (Figure S6a). All three electrodes showed good surface wettability; however, the thickest (5L) electrode showed the lowest mean contact angle of 6.34° with the electrolyte droplet, indicating strong surface wettability whereas the 3 and 1L had a mean contact angles of 8.42° and 13.47° respectively. This further demonstrates the efficient ion transport and improved battery performance of 5L-thick electrodes compared to those of 3L and 1L electrodes. The contact angle variation of the electrolyte droplet on the surface of the 5L-thick electrode over 300 ms is shown in Figure 4i.

It has been reported that the dry-coated thick electrode possesses stability issues during long-term operation of the cells [33, 34]. Taking advantage of the unique strategy of combining the binder with the graphene-based conductive additives and fast electrolyte absorption, these dry-processed electrodes were subjected to various electrochemical tests to realize the efficacy of rGO over other conducting additives in multilayer dry-coated electrodes. In addition, the electrochemical performance of the dry cathodes was compared with that of wet-processed cathodes.

Notably, dry cathodes comprising rGO demonstrate a higher specific capacity and rate performance than those prepared by the slurry method. The significant enhancement in the performance of rGO-based dry cathodes is attributed to the formation of a

21983844, 0, Downloaded from https://advanced.onlinelibrary.wiley.com/doi/10.1002/advs.78763 by Statens Beredning, Wiley Online Library on [16/11/2026]. See the Terms and Conditions (https://onlinelibrary.wiley.com/terms-and-conditions) on Wiley Online Library for rules of use; OA articles are governed by the applicable Creative Commons License

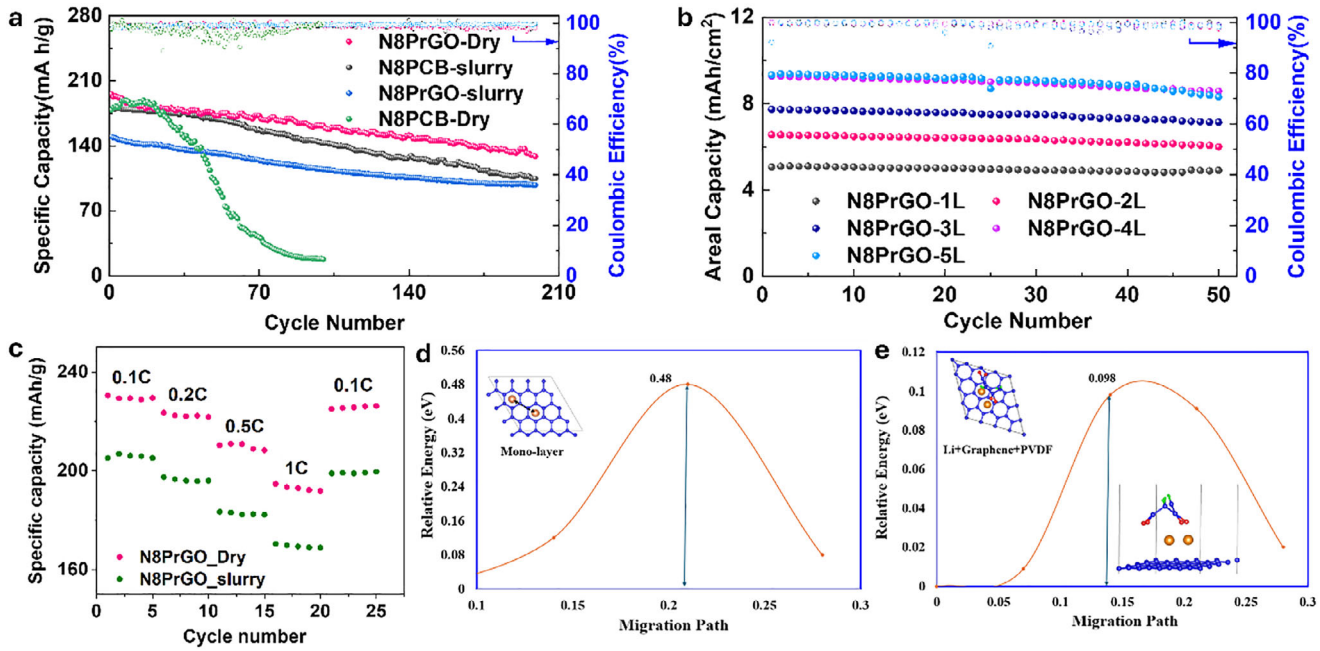


FIGURE 5 | (a) Cycling performance of dry-coated N8PrGO (2L), N8PCB, and slurry-coated cathode under constant-current charge–discharge test at 0.2C; (b) The areal capacity variation as a function of cycle number for 1 to 5L thick N8PrGO cathodes; (c) Rate performance comparison of dry coated (1L) and slurry-based NMC811 electrode; Energy barrier for Li-ion diffusion on (d) monolayer graphene, and (e) graphene with PVDF.

strong 3D interconnected network with PVDF, allowing for better electrolyte infiltration and improved electron and ion conducting pathways and efficient utilization of active material. Figure 5a represents the cycling performance of cathodes prepared by the dry and slurry processes using rGO and CB as conducting fillers. The dry N8PrGO (2L) exhibits excellent cycling performance with 80% capacity retention over 200 cycles, outperforming the slurry-based cathodes. On the other hand, dry cathodes with CB experience a rapid decline in capacity after about 40 cycles due to electrode fragmentation and binder carbon agglomeration, which results in poor electrolyte wettability and hence displays poor cyclic stability. However, the slurry-processed cathodes with CB displayed relatively better and comparable performance to that of rGO-based wet electrodes (Figure 5a). The electrochemical performance of the multilayer, dry-processed NMC811 electrodes incorporating the rGO–PVDF conductive binder formulation compares favorably with that of other dry-processed NMC-based cathodes reported in the literature (Table S1). Please note that the dry electrodes processed with GNP as a conducting additive showed agglomeration during the hot pressing, which hindered the effective binding between PVDF and NMC particles. Consequently, the films obtained from hot pressing of PVDF and NMC811 with GNP lack charge–discharge capabilities.

The cyclic voltammograms for the wet and dry electrodes shown in Figure S3a–c show typical reversible redox peaks corresponding to Ni^{2+}/Ni^{4+}, Mn^{3+}/Mn^{4+}, and Co^{3+}/Co^{4+}. It is evident from the CV plots that the dry-processed 1 and 2L cathodes displayed higher capacity and redox peak currents when compared to those of slurry-processed electrodes. The dQ/dV plots of the slurry and dry cathodes in Figure S4a,b indicate a stable electrochemical process occurring during charge–discharge without phase and structural changes. Even from this plot, it is evident that electrochemical processes and kinetics are much better for dry-processed electrodes when compared to those of wet electrodes. Figure 5c represents the rate performance of slurry- and dry-processed N8PrGO cathodes at different C-rates. The dry-processed N8PrGO cathode achieves a specific discharge capacity of 230 mAh/g at 0.1C and maintains over 190 mAh/g at 1C, significantly outperforming the slurry-processed cathodes, which displayed relatively lower specific capacities of 205 and 165 mA h/g at 0.1 and 1C, respectively. The larger specific surface area and porous structure of rGO allow for better electrolyte wettability and infiltration, resulting in faster Li-ion diffusion, thereby maintaining higher efficiency even at higher charge–discharge currents. The SEM images of N8PrGO cathodes before (Figure S5b) and after (Figure S5c) cycling show no significant changes in morphology, indicating their excellent stability over several charge–discharge cycles.

Considering the improved electrochemical performance of rGO-based dry electrodes, in the next set of experiments we fabricated LIBs with increased areal loading of active material from 20 to 90 mg/cm^2 to further demonstrate the efficacy of our layer-by-layer additive manufacturing approach. The electrochemical impedance spectroscopy (EIS) plots for 1- and 5L-thick electrodes showed charge transfer resistance (R_{ct}) of 40 and 100 Ω, respectively (Figure S7). Upon charge and discharge, the R_{ct} values reduced significantly, indicating faster electrode kinetics and ion diffusion at the CEI. The percentage decrease in R_{ct} for 5L-thick electrodes is higher when compared to that of 1L cathodes, and hence they exhibit better electrochemical performance. Figure 5b presents the active material loading range of 1–5-layer dry-processed N8PrGO cathodes and their areal discharge capacity in the range of 5 (1L)–9 mAh/cm^2 (5L) with stability over 50 charge–discharge cycles. At the 20th cycle, the areal discharge capacity of the cathode material is directly proportional to its loading

21983844, 0, Downloaded from https://advanced.onlinelibrary.wiley.com/doi/10.1002/advs.78763 by Statens Beredning, Wiley Online Library on [16/11/2026]. See the Terms and Conditions (https://onlinelibrary.wiley.com/terms-and-conditions) on Wiley Online Library for rules of use; OA articles are governed by the applicable Creative Commons License

(Figure S8), indicating that with increasing layers, the electrode thickness and loading increase while maintaining a specific discharge capacity above 210 mAh/g. This demonstrates that the layer-by-layer coating and multiple hot-pressing technique proposed in this study effectively maintain the active material utilization rate in high-loading thick electrodes. The high specific surface area structure provided by rGO allows deep electrode NMC particles to be fully utilized, and no layer interfaces that could affect battery capacity are formed in the cathodes obtained from multiple powder layering and hot pressing. The dry multilayer hot-pressing technique proposed in this study can be used to fabricate cathodes with loadings above 50 mg/cm^2 with an areal discharge capacity exceeding 9 mA h/cm^2. At high electrode loadings, fabricating a uniform thick electrode using a single powder-deposition step is challenging because of powder spreading and limited control over the final electrode dimensions and thickness. In addition, the electrodes with the same mass loading (e.g., ca. 47 mg/cm^2) but prepared using different coating times (1-, 3-, and 5-times) also show different electrochemical performance. As shown in Figure S9, the high mass loading electrode coated with 1 layer exhibited lower capacity and a pronounced capacity drop after approximately 41 cycles, indicating insufficient electrode adhesion and structural stability. In contrast, the same high mass loading electrodes using 3 and 5L delivered comparable capacities, while the 5L electrode exhibited improved cycling stability. These results demonstrate that the layer-by-layer deposition and hot-compaction strategy enhances electrode integrity and stability, facilitating effective active-material utilization and reliable performance in high-loading dry electrodes. Thus, this multilayer additive manufacturing approach is of high importance to develop high energy density LIBs with high mass loading of active material and has the potential to be extended to develop dry coating for other electrode materials like LFP, LMFP, and other battery chemistry and can be integrated with standard anode materials and solid electrolytes [35, 36]. Previous studies have reported that electrolyte availability and lithium-metal-anode stability can influence the long-term cycling performance of ultrahigh-loading electrodes [37–39].

To further demonstrate the versatility and potential industrial relevance of the proposed manufacturing strategy, dry N8PrGO electrodes with reduced rGO/PVDF contents of 5 wt.% and 2.5 wt.% were fabricated and evaluated electrochemically. Both formulations exhibited comparable specific capacities and stable cycling performance over 100 cycles (Figure S10), demonstrating that the multilayer dry-electrode process can accommodate reduced inactive-material contents without compromising electrochemical stability. Furthermore, the process was extended to LFP and NMC111 cathodes, whose cells exhibited high specific capacities and stable cycling performance over 100 cycles (Figure S11), highlighting the applicability of the proposed strategy to different cathode chemistries.

2.3 | Li-Ion Diffusion Mechanism in Graphene Layers

To analyze the Li-ion diffusion across multiple graphene layers, minimum energy diffusion paths and activation energies were considered through the Nudged Elastic Band (NEB) method [40, 41]. The obtained energy profile is shown in Figure 5d,e, whereas the structural evolution based on the Ab Initio Molecular Dynamics (AIMD) simulations at 25°C and high temperature (180°C) is depicted in Figure 3c,d. The activation barrier of Li-ion migration on pure monolayer graphene is relatively high (0.48 eV), which implies that Li is strongly localized at adsorption sites on the surface of graphene (Figure S6b). This energy barrier indicates the restriction of longer Li-ion diffusion paths since the Li-ion interacts strongly with the π -electron cloud of the graphene sheet. Upon introduction of the PVDF matrix, the Li-ion diffusion profile has significantly changed. The NEB energy profile of Li^+ on graphene and graphene (Figure 5d) with PVDF (Figure 5e) shows that the migration barrier is considerably lower (0.098 eV), which shows that the PVDF domains favor the transportation of Li-ions across the surface of the graphene. This enhancement originates from the polar β-phase PVDF chains, where the aligned C–F dipoles weaken Li–graphene binding and create a smoother electrostatic potential, thereby lowering the diffusion barrier. AIMD simulations were also performed at 180°C to mimic the experimental conditions. It is evident from the optimized geometries at 180°C that there existed a strong chemisorption between a polymeric network of PVDF and graphene, which in turn promotes faster Li-ion diffusion. These findings validate the high interfacial interaction and thermal strength of the PVDF-graphene mixture.

The standard Arrhenius equation was used to estimate the Li-ion diffusion coefficient in the dry coated thick electrode,

$$D_{\mathrm{Li}}(T) = D_0 \exp\left(-E_A/k_B T\right),$$

where E_A is the diffusion barrier obtained from the energy profile and D_0 is the pre-exponential factor. Using $D_0 = 1.56 \times 10^{-7}$ m^{2}s^{-1}, with the lowest barrier found between the PVDF and graphene system, the Li-ion diffusion coefficient is estimated to be 3.5×10^{-5} m^{2}s^{-1}. On pure graphene, the diffusion coefficient is around 1.3×10^{-11} m^{2}s^{-1}. The six orders of magnitude higher Li-ion diffusion is attributed to the strong PVDF-rGO binding, which promotes faster Li-ion mobility across the graphene layers facilitated by the amorphous PVDF domains. Further AIMD simulations at room temperature (300 K) also validate the structural stability of the PVDF and PVDF-graphene interface.

The interfaces of NMC811(104)/PVDF and NMC811(104)/rGO/PVDF were constructed to examine the effect of rGO on the stability of the interface and Li-ion transport, to mimic the realistic electrode environment (Figure S12). Compared to NMC811/PVDF, the calculated binding energy of NMC811/rGO/PVDF is −2.31 eV, which is significantly larger for the latter. The calculated binding energy is stronger for NMC811/rGO/PVDF than for NMC811/PVDF, and is found to be −1.42 and −2.31 eV, respectively. Besides, the CI-NEB calculations show that the migration barrier of Li-ion goes down from 0.64 (NMC811/PVDF interface) to 0.38 eV (NMC811/rGO/PVDF interface). It is found that rGO can lower the electrode interface energy loss by ∼0.26 eV, which not only stabilizes the heterogeneous electrode interface but also offers a more favorable local energy landscape for Li-ion migration. The results explain the improvements in charge/ion transport at the interface due to the rGO/PVDF conductive-binder architecture at the atomic level.

21983844, 0, Downloaded from https://advanced.onlinelibrary.wiley.com/doi/10.1002/advs.78763 by Statens Beredning, Wiley Online Library on [16/11/2026]. See the Terms and Conditions (https://onlinelibrary.wiley.com/terms-and-conditions) on Wiley Online Library for rules of use; OA articles are governed by the applicable Creative Commons License

3 | Conclusion

In this work, we report a solvent-free, roll-to-roll hot-pressing route combined with layer-by-layer additive manufacturing dry powder coating, which enabled the scalable fabrication of high mass loading NMC 811 with controlled thickness (300–1100 μm) and areal loading (20–100 mg cm^{-2}). The rGO-PVDF interaction during hot pressing produces a continuous, mechanically reinforced conductive binding network that strongly interacts with NMC particles, suppressing binder aggregation and improving the interparticle adhesion and electronic pathways. These multilayered electrodes delivered a high specific capacity of ~230 mAh g^{-1} at 0.1C and areal capacities up to 9 mAh cm^{-2} with active material loading exceeding 50 mg cm^{-2}. The synergistic interaction between PVDF and rGO was the key to achieve both structural integrity and stable electrochemical performance. These performance metrics demonstrate a practical pathway to high-energy cathodes that are compatible with continuous roll-to-roll industrial production while reducing energy consumption and cost by avoiding the use of toxic solvents like NMP. The process is chemistry-agnostic (validated on NMC811 and extendable to NMC111 and LFP) and is well suited for pairing with high-capacity anodes and for integration with solid-state electrolytes. As an extension, optimizing rGO content and calendaring parameters for thicker stacks and investigations on electrolyte infiltration and interphase formation under high-rate, long-cycle conditions are of high interest. Furthermore, validation of our dry electrode manufacturing approach for developing pouch-/cylindrical cell-level prototypes on pilot roll-to-roll lines will be of great interest for large-scale production of high energy density lithium-ion batteries.

Author Contributions

Tianlin Zhang: methodology, data curation, investigation, validation, formal analysis, writing – original draft. **Bharathkumar H. Javaregowda:** methodology, data curation, investigation, validation, formal analysis, writing – original draft. **Prince M. Paul:** methodology, data curation, formal analysis, DFT simulations. **Ravi Trivedi:** methodology, data curation, formal analysis, DFT simulations. **Till Dreier:** methodology, formal analysis, data curation. **Eduard Hryha:** methodology, writing – review and editing, validation. **Lars Nyborg:** methodology, investigation, writing – review and editing, validation. **Gao Liu:** methodology, investigation, writing – review and editing, validation. **Jinhua Sun:** conceptualization, methodology, investigation, validation, supervision, formal analysis, funding acquisition, project administration, resources, writing – original draft, writing – review and editing.

Acknowledgements

This work was funded by the Vinnova project (2023-02551), Swedish Energy Agency (Energimyndigheten) (P2023-01041), and the VINNOVA competence Centre (2019-00068). We acknowledge the support from COMPEL (Competence and Excellence in Battery Research and Education for the Transport Sector), Centre for Battery Manufacturing, Products and Systems (MAXBATT), and the Chalmers Production Area of Advance. We also acknowledge the support of the Transportation Technologies Office (TTO) of the U.S. Department of Energy (US DOE). The authors acknowledge Mr. Stefan Benn & Mr. Malte Snoyek from KRÜSS GmbH, Hamburg, for electrolyte absorption measurements.

Conflicts of Interest

The authors declare no conflicts of interest.

Data Availability Statement

The data that support the findings of this study are available from the corresponding author upon reasonable request.

References

1. McKinsey & Company *Lithium-Ion Battery Demand Forecast for 2030* (McKinsey & Company, 2023).

2. Y. Li, Y. Wu, Z. Wang, et al., "Progress in Solvent-Free Dry-Film Technology for Batteries and Supercapacitors," *Materials Today* 55 (2022): 92–109, https://doi.org/10.1016/j.mattod.2022.04.008.

3. J. Yu, B. Kim, and Y. Yoo, "Dry Electrode Processing for Lithium-Ion Battery Cathodes and Anodes: Materials, Fabrication Strategies, and Future Outlook," *Advanced Materials Technologies* 10, no. 22 (2025): 01420, https://doi.org/10.1002/admt.202501420.

4. J. Choi, S. Moon, D. Lee, et al., "Dry Electrode Technology: A New Processing Paradigm for Enhancing Performance and Sustainability in Lithium-Based Batteries," *Chemical Engineering Journal* 519 (2025): 165044, https://doi.org/10.1016/j.cej.2025.165044.

5. K. Turcheniuk, D. Bondarev, G. G. Amatucci, and G. Yushin, "Battery Materials for Low-Cost Electric Transportation," *Materials Today* 42 (2021): 57–72, https://doi.org/10.1016/j.mattod.2020.09.027.

6. H. Hagiwara, W. J. Suszynski, and L. F. Francis, "A Raman Spectroscopic Method to Find Binder Distribution in Electrodes During Drying," *Journal of Coatings Technology and Research* 11 (2013): 11–17, https://doi.org/10.1007/s11998-013-9509-z.

7. B. Johansson, M. Despeisse, J. Bokrantz, et al., "Challenges and Opportunities to Advance Manufacturing Research for Sustainable Battery Life Cycles," *Frontiers in Manufacturing Technology* 4 (2024): 1360076, https://doi.org/10.3389/FMTEC.2024.1360076.

8. G. Schälicke, I. Landwehr, A. Dinter, K. H. Pettinger, W. Haselrieder, and A. Kwade, "Solvent-Free Manufacturing of Electrodes for Lithium-Ion Batteries via Electrostatic Coating," *Energy Technology* 8, no. 2 (2020): 1900309, https://doi.org/10.1002/ente.201900309.

9. M. Ryu, Y. K. Hong, S. Y. Lee, and J. H. Park, "Ultrahigh Loading Dry-Process for Solvent-Free Lithium-Ion Battery Electrode Fabrication," *Nature Communications* 14, no. 1 (2023): 1316, https://doi.org/10.1038/s41467-023-37009-7.

10. F. Wu, Q. Shi, L. Chen, et al., "New Insights Into Dry-Coating-Processed Surface Engineering Enabling Structurally and Thermally Stable High-Performance Ni-Rich Cathode Materials for Lithium Ion Batteries," *Chemical Engineering Journal* 470 (2023): 144045, https://doi.org/10.1016/j.cej.2023.144045.

11. Y. Liu, X. Gong, C. Podder, et al., "Roll-to-Roll Solvent-Free Manufactured Electrodes for Fast-Charging Batteries," *Joule* 7, no. 5 (2023): 952–970, https://doi.org/10.1016/j.joule.2023.04.006.

12. B. Ludwig, Z. Zheng, W. Shou, Y. Wang, and H. Pan, "Solvent-Free Manufacturing of Electrodes for Lithium-Ion Batteries," *Scientific Reports* 6, no. 1 (2016): 23150, https://doi.org/10.1038/srep23150.

13. K. Uzun, H. Alolaywi, S. Thapa, et al., "Investigating the Effect of Electrode Compositions on Dry-Made NMC811 Positive Electrodes," *Journal of The Electrochemical Society* 171, no. 8 (2024): 080532, https://doi.org/10.1149/1945-7111/ad6cfb.

14. D. J. Kirsch, S. D. Lacey, Y. Kuang, et al., "Scalable Dry Processing of Binder-Free Lithium-Ion Battery Electrodes Enabled by Holey Graphene," *ACS Applied Energy Materials* 2, no. 5 (2019): 2990–2997, https://doi.org/10.1021/acsaem.9b00066.

15. I. Hwang, K. E. Sung, J. Hong, G. S. Kang, and J. Yoon, "A Breakthrough in Dry Electrode Technology for High-Energy-Density Lithium-Ion Batteries With Spray-Dried SWCNT/NCM Composites,"

21983844, 0, Downloaded from https://advanced.onlinelibrary.wiley.com/doi/10.1002/advs.78763 by Statens Beredning, Wiley Online Library on [16/11/2026]. See the Terms and Conditions (https://onlinelibrary.wiley.com/terms-and-conditions) on Wiley Online Library for rules of use; OA articles are governed by the applicable Creative Commons License

Chemical Engineering Journal 506 (2025): 160159, https://doi.org/10.1016/j.cej.2025.160159.

16. M. Zhang, B. K. Stoychev, X. Zhang, et al., "Dry Electrode Architecture Design to Push Energy Density Limits at the Cell Level," *Nature Energy* 11, no. 3 (2026): 490–502, https://doi.org/10.1038/s41560-026-01981-3.

17. R. Li, X. Jin, B. H. Javaregowda, J. Sun, and G. Liu, "Structured for Success: Conjugated Polymer Binders With Tailored Composition and Architecture for Lithium-Ion Batteries," *EES Batteries* 2 (2026): 112–129, https://doi.org/10.1039/D5EB00175G.

18. D. Lee, Y. Shim, Y. Kim, et al., "Shear Force Effect of the Dry Process on Cathode Contact Coverage in All-Solid-State Batteries," *Nature Communications* 15 (2024): 4763, https://doi.org/10.1038/s41467-024-49183-3.

19. Process for Producing a Dry Film and Dry Film and Dry Film Coated Substrate, DE102017208220A1 (2017).

20. Danish Environmental Protection Agency *Survey Of Selected Fluorinated Greenhouse Gases* (Danish Environmental Protection Agency, 2014).

21. P. Purohit and L. Höglund-Isaksson, "Global Emissions of Fluorinated Greenhouse Gases 2005–2050 With Abatement Potentials and Costs," *Atmospheric Chemistry and Physics* 17, no. 4 (2017): 2795–2816, https://doi.org/10.5194/acp-17-2795-2017.

22. R. Diehm, M. Müller, D. Burger, et al., "High-Speed Coating of Primer Layer for Li-Ion Battery Electrodes by Using Slot-Die Coating," *Energy Technology* 8, no. 9 (2020): 2000259, https://doi.org/10.1002/ente.202000259.

23. S. Han, E. H. Noh, S. Chae, et al., "Mitigating PTFE Decomposition in Ultra Thick Dry-Processed Anodes for High Energy Density Lithium-Ion Batteries," *Journal of Energy Storage* 96 (2024): 112693, https://doi.org/10.1016/j.est.2024.112693.

24. Y. Suh, J. K. Koo, H. ji Im, and Y. J. Kim, "Astonishing Performance Improvements of Dry-Film Graphite Anode for Reliable Lithium-Ion Batteries," *Chemical Engineering Journal* 476 (2023): 146299, https://doi.org/10.1016/j.cej.2023.146299.

25. L. Guobao, X. Rongjian, and L. Chen, "The Influence of Polytetrafluorethylene Reduction on the Capacity Loss of the Carbon Anode for Lithium Ion Batteries," *Solid State Ionics* 90 (1996): 221–225, https://doi.org/10.1016/s0167-2738(96)00367-0.

26. R. Tao, B. Steinhoff, C. H. Sawicki, et al., "Unraveling the Impact of the Degree of Dry Mixing on Dry-Processed Lithium-Ion Battery Electrodes," *Journal of Power Sources* 580 (2023): 233379, https://doi.org/10.1016/j.jpowsour.2023.233379.

27. M. P. Shilpa, B. Chethan, S. J. Shetty, et al., "Highly Responsive Reduced Graphene Oxide Embedded PVDF Flexible Film-Based Room Temperature Operable Humidity Sensor," *Sensors and Actuators A: Physical* 366 (2024): 115011, https://doi.org/10.1016/j.sna.2024.115011.

28. M. Sieradzka, R. Fryczkowski, D. Biniaś, W. Biniaś, and J. Janicki, "A Facile Approach to Obtaining PVDF/Graphene Fibers and the Effect of Nanoadditive on the Structure and Properties of Nanocomposites," *Polymer Testing* 81 (2020): 106229, https://doi.org/10.1016/j.polymertesting.2019.106229.

29. L. Wu, W. Yuan, N. Hu, et al., "Improved Piezoelectricity of PVDF-HFP/Carbon Black Composite Films," *Journal of Physics D: Applied Physics* 47, no. 13 (2014): 135302, https://doi.org/10.1088/0022-3727/47/13/135302.

30. J. Wang, M. Yi, Z. Shen, L. Liu, X. Zhang, and S. Ma, "Enhanced Thermal and Mechanical Properties of Poly (Vinylidene Fluoride) Nanocomposites Reinforced by Liquid-Exfoliated Graphene," *Journal of Macromolecular Science, Part A* 56, no. 7 (2019): 733–740, https://doi.org/10.1080/10601325.2019.1607375.

31. I. O. Pariy, A. A. Ivanova, V. V. Shvartsman, et al., "Piezoelectric Response in Hybrid Micropillar Arrays of Poly(Vinylidene Fluoride) and Reduced Graphene Oxide," *Polymers* 11, no. 6 (2019): 1065, https://doi.org/10.3390/POLYM11061065.

32. A. Gutiérrez, N. Alomari, S. Aparicio, et al., "Understanding of Three Different Polyvinylpyrrolidone (PVP) Based Battery Binders Blends on Graphene Surfaces From First Principles via DFT Simulations," *Materials Chemistry and Physics* 301 (2023): 127548, https://doi.org/10.1016/j.matchemphys.2023.127548.

33. Integrated One-Step Dry Process Enabling Prelithiated Thick Electrodes Without Primer Coating for High Energy Density and Initial Coulombic Efficiency *Energy & Environmental Science* 19 6, (2026): 1944–1953, https://doi.org/10.1039/d5ee05739f.

34. H. Jung and Y. Yoo, "Thick Electrodes for High-Energy Lithium-Ion Batteries: Structural Limitations, Wet/Dry Process Engineering, and Integrated Design Strategies," *Journal of Power Sources* 670 (2026): 239528, https://doi.org/10.1016/J.JPOWSOUR.2026.239528.

35. Y. Sun, J. Sun, J. S. Sanchez, et al., "Surface Chemistry and Structure Manipulation of Graphene-Related Materials to Address the Challenges of Electrochemical Energy Storage," *Chemical Communications* 59, no. 18 (2023): 2571–2583, https://doi.org/10.1039/D2CC06772B.

36. R. Chen, N. M. Santhosh, J. Zavasnik, et al., "Plasma Surface Engineering of Graphite and Its Effect on Advancing the Performance of Aluminium Battery," *Carbon* 245 (2025): 120835, https://doi.org/10.1016/J.CARBON.2025.120835.

37. X. Li, Y. Rao, S. Zhao, et al., "Fluorosulfonyl Additive-Reinforced Interphases for High-Voltage and Fast-Charging Lithium Metal Batteries," *ACS Applied Materials & Interfaces* 18, no. 35 (2026): 47565–47577, https://doi.org/10.1021/ACSAMI.6C07324.

38. C. C. Su, X. Wu, K. Amine, and M. V. Bracamonte, "Probing the Effectiveness in Stabilizing Lithium Metal Anodes Through Functional Additives," *ACS Applied Materials & Interfaces* 15, no. 50 (2023): 59016–59024, https://doi.org/10.1021/ACSAMI.3C14119.

39. M. Alhajj, N. Attan, A. Abedelqader, M. Aziz, and S. A. setu, "Suppressing Dendritic Growth in Lithium Metal Batteries: Recent Strategies, Mechanistic, and Technological Advances," *Journal of Power Sources* 660 (2025): 238520, https://doi.org/10.1016/J.JPOWSOUR.2025.238520.

40. G. Henkelman, B. P. Uberuaga, and H. Jónsson, "A Climbing Image Nudged Elastic Band Method for Finding Saddle Points and Minimum Energy Paths," *The Journal of Chemical Physics* 113, no. 22 (2000): 9901–9904, https://doi.org/10.1063/1.1329672.

41. J. Sun, M. Sadd, P. Edenborg, et al., "Real-Time Imaging of Na^+ Reversible Intercalation in "Janus" Graphene Stacks For Battery Applications," *Science Advances* 7, no. 22 (2021): 812–840, https://doi.org/10.1126/SCIADV.ABF0812;CTYPE:STRING:JOURNAL.

Supporting Information

Additional supporting information can be found online in the Supporting Information section.

Supporting File: advs78763-sup-0001-SuppMat.docx.

21983844, 0, Downloaded from https://advanced.onlinelibrary.wiley.com/doi/10.1002/advs.78763 by Statens Beredning, Wiley Online Library on [16/11/2026]. See the Terms and Conditions (https://onlinelibrary.wiley.com/terms-and-conditions) on Wiley Online Library for rules of use; OA articles are governed by the applicable Creative Commons License